

**A biomimetic all-inorganic photocatalyst for the artificial photosynthesis of hydrogen peroxide**

Journal:	<i>Catalysis Science &amp; Technology</i>
Manuscript ID	CY-ART-06-2022-001089.R1
Article Type:	Paper
Date Submitted by the Author:	18-Aug-2022
Complete List of Authors:	Teranishi, Miwako; Kindai University Naya, Shin-ichi; Kindai University Yan, Yaozong; Kindai University, Molecular Engineering Institute Soejima, Tetsuro; Kindai University, Department of Applied Chemistry Kobayashi, Hisayoshi; Kyoto Institute of Technology, Tada, Hiroaki; Kindai University, Molecular Engineering Institute

# Catalysis Science & Technology

## A biomimetic all-inorganic photocatalyst for the artificial photosynthesis of hydrogen peroxide

Received 00th January 20xx,  
Accepted 00th January 20xx

Miwako Teranishi,<sup>a</sup> Shin-ichi Naya,<sup>a</sup> Yaozong Yan,<sup>b</sup> Tetsuro Soejima,<sup>b</sup> Hisayoshi Kobayashi,<sup>c</sup> and Hiroaki Tada<sup>\*b</sup>

DOI: 10.1039/x0xx00000x

The artificial photosynthesis of H<sub>2</sub>O<sub>2</sub> from water and O<sub>2</sub> presents a sustainable route for the production. Remarkable progress in the rate of reaction has recently been achieved mainly by using semiconducting organic polymer photocatalysts. In view of the use under harsh oxidative conditions, the development of robust inorganic photocatalysts is highly desired. Here we present a photocatalyst with the unit consisting of a single Au particle and an interconnected cluster of SnO<sub>2</sub> nanocrystals with the surface modified by SbCl<sub>3</sub> (Au@SnO<sub>2</sub>-Sb(III)). Under visible-light irradiation ( $\lambda_{\text{ex}} = 420 \text{ nm}$ ), Au@SnO<sub>2</sub>-Sb(III) stably produces H<sub>2</sub>O<sub>2</sub> with a rate of 6.1 mM g<sup>-1</sup> h<sup>-1</sup> and an external quantum yield of 1.1%. This striking photocatalytic activity of Au@SnO<sub>2</sub>-Sb(III) originates from the action of SnO<sub>2</sub>-Sb(III) as a “light antenna” and “electron transporter”, the electrocatalytic activity of Au NPs for two electron–oxygen reduction reaction, the visible-light induced activity of SnO<sub>2</sub>-Sb(III) for oxygen evolution reaction, the weak adsorptivity for H<sub>2</sub>O<sub>2</sub>, and the robustness.

### Introduction

Hydrogen peroxide (H<sub>2</sub>O<sub>2</sub>) is not only a very useful clean oxidant for organic synthesis<sup>1</sup> and water purification<sup>2</sup> but also a hopeful fuel for fuel cells.<sup>3–6</sup> Presently, most H<sub>2</sub>O<sub>2</sub> is industrially produced by the energy-consuming anthraquinone autoxidation *via* the multi-steps. As the alternatives, various chemical and physical methods for H<sub>2</sub>O<sub>2</sub> production have recently been intensively studied.<sup>7</sup> Among them, the solar-to-H<sub>2</sub>O<sub>2</sub> conversion from earth-abundant water and O<sub>2</sub> can be a promising artificial photosynthesis to be challenged in chemistry (Eq. 1).<sup>8,9</sup>



The photocatalyst for efficient H<sub>2</sub>O<sub>2</sub> synthesis should possess the following features: (1) visible-light responsiveness, (2) efficient charge separation, catalytic activities for (3) oxygen evolution reaction (OER) and (4) two electron–oxygen reduction reaction (2e<sup>-</sup>-ORR), (5) weak adsorptivity for H<sub>2</sub>O<sub>2</sub>, and (6) high stability. Recently, various semiconducting polymer photocatalysts with high conversion efficiency have been developed.<sup>10,11</sup> However, these materials can undergo degradation because the photocatalytic synthesis of H<sub>2</sub>O<sub>2</sub> is accompanied by the

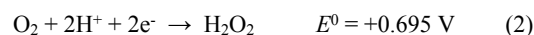
for the H<sub>2</sub>O<sub>2</sub> production from water and O<sub>2</sub> reported so far are only limited to the systems including Au/TiO<sub>2</sub><sup>14</sup>, Au/WO<sub>3</sub><sup>15,16</sup>, Au/BiVO<sub>4</sub><sup>17</sup>, graphene oxide<sup>17</sup>, N-doped Cu<sub>2</sub>O@Cu<sup>18</sup>, Pt-PtO<sub>x</sub>/WO<sub>3</sub><sup>19</sup>, and Pd/Mo:BiVO<sub>4</sub>/CoO<sub>x</sub>.<sup>20</sup> However, no photocatalyst satisfying all the requirements has been developed to date, and in most of the systems, the rate of H<sub>2</sub>O<sub>2</sub> production remains lower than ~2 mM g<sup>-1</sup> h<sup>-1</sup> (Table S1†).

In this study, an all-inorganic hybrid photocatalyst mimicking the natural photosynthesis<sup>21</sup> has been designed to enhance the photocatalytic activity. The photocatalyst with the unit structure consisting of a single Au NP (~50 nm) and an interconnected cluster (> ~100 nm) of many antimony chloride-surface modified SnO<sub>2</sub> nanocrystals (NCs, ~30 nm) (Au@SnO<sub>2</sub>-Sb(III)). Au@SnO<sub>2</sub>-Sb(III) has been shown to fulfil the requirements (1)–(6), stably producing H<sub>2</sub>O<sub>2</sub> from water and O<sub>2</sub> with a rate of 6.1 mM g<sup>-1</sup> h<sup>-1</sup> and an external quantum efficiency over 1% at  $\lambda_{\text{ex}} = 420 \text{ nm}$ . To our knowledge, this is the first report on the H<sub>2</sub>O<sub>2</sub> production from water and O<sub>2</sub> by SnO<sub>2</sub>-based photocatalysts.

### Results and discussion

H<sup>+</sup>-coupled 2e<sup>-</sup>-ORR directly yields H<sub>2</sub>O<sub>2</sub> in the reduction process of the photocatalytic H<sub>2</sub>O<sub>2</sub> synthesis (Eq. 2), where  $E^0$  denotes the standard redox potential with respect to the standard hydrogen electrode (SHE).<sup>22</sup> Also, H<sub>2</sub>O<sub>2</sub> can be produced via one electron-ORR (Eqs. 3–5), but the resulting O<sub>2</sub><sup>•-</sup> undergoes oxidation by the holes to generate singlet oxygen (<sup>1</sup>O<sub>2</sub>, Eq. 6).<sup>23</sup>

#### Reduction processes



#### Oxidation process



<sup>a</sup> Environmental Research Laboratory, Kindai University, 3-4-1, Kowakae, Higashi-Osaka, Osaka 577-8502, Japan.

<sup>b</sup> Graduate School of Science and Engineering, Kindai University, 3-4-1, Kowakae, Higashi-Osaka, Osaka 577-8502, Japan.

<sup>c</sup> Emeritus Prof. Kyoto Institute of Technology, Matsugasaki, Sakyo-ku, Kyoto, 606-8585, Japan.

† Footnotes relating to the title and/or authors should appear here.

Electronic Supplementary Information (ESI) available: [details of any supplementary information available should be included here]. See DOI: 10.1039/x0xx00000x

generation of activated oxygen species damaging the organic structures.<sup>12</sup> For the use under the harsh oxidative conditions, robust inorganic metal oxide-based photocatalysts are more favourable.<sup>13</sup> The metal oxide-based visible-light photocatalysts



Thus, the conduction band (CB) edge potential of the metal oxide (MO) photocatalyst should be situated between -0.330 V and +0.695 V

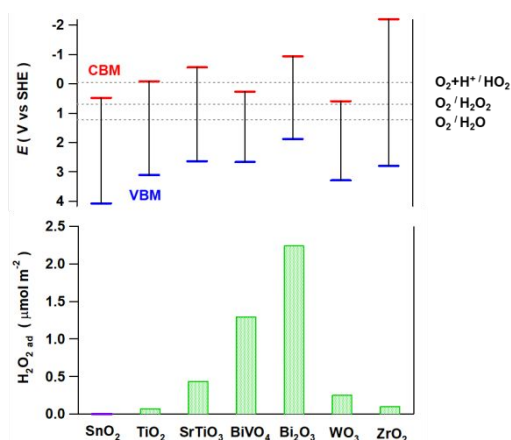


**Fig. 1.** Band edge potentials of various metal oxides with respect to the redox potentials of water and O<sub>2</sub> (upper). Saturated adsorption amount of H<sub>2</sub>O<sub>2</sub> on various metal oxides at 298 K (lower).

V to increase the selectivity for 2e<sup>-</sup>-ORR by inhibiting one electron-ORR. Simultaneously, the VB edge potential of the MO semiconductor should be more positive than the potential for OER of +1.229 V (Eq. 7). Among various MOs, SnO<sub>2</sub>, WO<sub>3</sub>, and BiVO<sub>4</sub> satisfy these conditions (Fig. 1, upper). On the other hand, the oxidation of H<sub>2</sub>O<sub>2</sub> ( $E^0(\text{O}_2/\text{H}_2\text{O}_2) = +0.695 \text{ V}$ ) more easily occur than OER ( $E^0(\text{O}_2/\text{H}_2\text{O}) = +1.229 \text{ V}$ ), while H<sub>2</sub>O<sub>2</sub> adsorbed on MOs is apt to reductive decomposition during the photocatalytic process.<sup>24</sup> To break through this thermodynamically unsolvable problem, the adsorption of H<sub>2</sub>O<sub>2</sub> on the photocatalyst must be suppressed. Then, the adsorption amount of H<sub>2</sub>O<sub>2</sub> on various MOs were measured (Table S2†). The adsorption amount of H<sub>2</sub>O<sub>2</sub> varies greatly depending on the type of MOs, and the adsorption capacity of SnO<sub>2</sub> to H<sub>2</sub>O<sub>2</sub> is particularly low (Fig. 1, lower). Additionally, SnO<sub>2</sub> has an extraordinary physicochemical stability, and then, it was selected as the base MO semiconductor for the photocatalyst in this study. On the other hand, Au NP<sup>14,25,26</sup> and Au-Ag alloy NPs<sup>27</sup> are promising electrocatalysts for 2e<sup>-</sup>-ORR because of its excellent activity. However, Au NP is catalytically active also for the decomposition of H<sub>2</sub>O<sub>2</sub>. In the design for the photocatalyst with Au NPs for H<sub>2</sub>O<sub>2</sub> production, the use of large Au NPs with small surface area is crucial to minimize the loss of H<sub>2</sub>O<sub>2</sub>.<sup>25</sup>

SbCl<sub>3</sub> was adsorbed on SnO<sub>2</sub> NCs with particle size ~30 nm and specific surface area = 100 m<sup>2</sup> g<sup>-1</sup> (FUJIFILM Wako Pure Chemical Co.) from the methanol solutions with various concentrations (SnO<sub>2</sub>-Sb(III)), and the amount of the adsorbed Sb ions were quantified by inductively coupled plasma (ICP) spectroscopy. The adsorption of SbCl<sub>3</sub> on SnO<sub>2</sub> NCs at 293 K apparently follows the Langmuir-type behavior with the adsorption amount ( $\Gamma_{\text{ad}}$ ) increasing in the equilibrium concentration ( $C_{\text{eq}}$ ) (Fig. S1a†). From the slope and intercept of the Langmuir plot, the saturated adsorption amount and adsorption equilibrium constant were calculated to be  $6.96 \times 10^{-1} \text{ mmol g}^{-1}$  and  $1.14 \times 10^3 \text{ M}^{-1}$ , respectively. The large adsorption equilibrium constant suggests strong chemisorption of SbCl<sub>3</sub> on SnO<sub>2</sub>.

The adsorption amount ( $\Gamma_{\text{ad}}$ ) can be precisely controlled by the initial concentration of SbCl<sub>3</sub> ( $C_0$ ) (Fig. S1b†).

In the high resolution-transmission electron microscopic (HR-TEM) image of unmodified SnO<sub>2</sub> (Fig. 2a), regularly aligned O-atom rows are observed. The d-spacing in the lattice fringe (3.35 Å) is in agreement with the value for the SnO<sub>2</sub>(110) crystal planes (3.35 Å) (ICDD No. 01-075-2893). Elemental mapping of SnO<sub>2</sub>-Sb(III) by the TEM-energy dispersive spectroscopic (EDS) (Fig. S2†) shows that Sb is uniformly distributed on the whole surface of SnO<sub>2</sub> NCs. In the HR-TEM image (Fig. 2b), many molecular scale dark spots are present on the O-atom rows, whereas the O-atom sequences are connected in the HR-TEM image for the unmodified SnO<sub>2</sub> (Fig. 2a). Further to study the state of the adsorbed Sb ions, Sb3d- and Cl2p-X-ray photoelectron (XP) spectra were measured. In the Sb3d-XP spectra of the samples with varying  $\Gamma_{\text{ad}}$  (Fig. 2c), two signals are observed at the binding energy ( $E_{\text{B}}$ ) = 540.1 eV and 530.7 eV assignable to the emission from the Sb3d<sub>3/2</sub> and Sb3d<sub>5/2</sub> orbitals of Sb(III) ions (Fig. S3†).<sup>28</sup> Both the signals intensify as a result of the increase in  $\Gamma_{\text{ad}}$  with the  $E_{\text{B}}$  values hardly changed. As shown by the Cl2p-XP spectra in (Fig. 2d), the samples have the Cl2p signals at  $E_{\text{B}}$  = 200.0 eV and 198.7 eV due to the emission from the Cl2p<sub>1/2</sub> and Cl2p<sub>3/2</sub> orbitals.<sup>28</sup> Clearly, SbCl<sub>3</sub> is adsorbed on SnO<sub>2</sub> while retaining some of the Cl<sup>-</sup> ligands. The Cl in the solution after the adsorption of SbCl<sub>3</sub> on SnO<sub>2</sub> NCs can exist as SbCl<sub>3</sub> and free Cl<sup>-</sup> ions. The mole numbers of Sb ( $n_{\text{s,Sb}}$ ) and Cl ( $n_{\text{s,Cl}}$ ) in the solutions were determined by ICP spectroscopy and ion chromatography, respectively. The subtraction of  $n_{\text{s,Cl}} - 3n_{\text{s,Sb}}$  yields the mole number of free Cl<sup>-</sup> ions in the solution ( $n_{\text{s,Cl}^-}$ ). Further, the number of Cl<sup>-</sup> ligands liberated by the adsorption ( $x$  in SbCl<sub>3-x</sub>) was calculated to be 1.6-2.0 by the ratio of  $n_{\text{s,Cl}^-}$  to the mole number of the Sb adsorbed on SnO<sub>2</sub> ( $n_{\text{ad,Sb}}$ ) (Fig. S4†). Diffuse reflectance infrared (DRIFT) spectra for SnO<sub>2</sub>-Sb(III) with varying  $\Gamma_{\text{ad}}$  were measured (Fig. S5†). In the spectrum of unmodified SnO<sub>2</sub>, a signal due to the stretching vibration of Sn<sub>s</sub>-OH groups is observed at 3700 cm<sup>-1</sup>, where Sn<sub>s</sub> denotes the surface Sn atom. The absorption intensity decreases

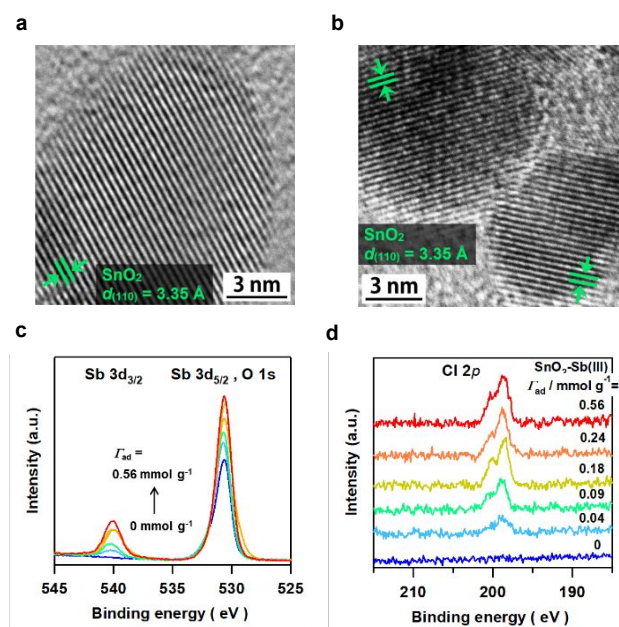
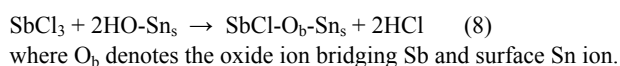


**Fig. 2.** (a) HR-TEM image of unmodified SnO<sub>2</sub>. (b) HR-TEM image of SnO<sub>2</sub>-Sb(III) prepared at  $C_0 = 50 \text{ mM}$ . (c) Sb3d (c) and Cl2p (d)-XP spectra of SnO<sub>2</sub>-Sb(III) with varying  $\Gamma_{\text{ad}}$ .

with the Sb(III)-surface modification, almost disappearing at  $\Gamma_{\text{ad}} = 0.56 \text{ mmol g}^{-1}$ . These results indicate that a mixed ligand surface complex is formed by the adsorption of  $\text{SbCl}_3$  on  $\text{SnO}_2$  via the ligand exchange between  $\text{Cl}^-$  ions and  $\text{Sn}_5\text{-OH}$  groups (Eq. 8).



This scheme is consistent with the presence of the dark spots on the O-atom rows in the  $\text{SnO}_2$  plane (Fig. 2b), and the density of the dark spots ( $> \sim 2 \text{ nm}^{-2}$ ) comparable with the value calculated from the adsorption amount of  $\text{SbCl}_3$  ( $2.6 \text{ nm}^{-2}$ ). Thus, the dark spots with highly dispersed at a molecular level in the HR-TEM image can be assigned to the  $\text{SbCl}$  species chemisorbed on  $\text{SnO}_2$ .

Diffuse reflectance spectra of  $\text{SnO}_2\text{-Sb(III)}$  with varying  $\Gamma_{\text{ad}}$  were measured. In the Kubelka-Munk transformed absorption spectra (Fig. 3a), unmodified  $\text{SnO}_2$  has absorption edge of  $\sim 400 \text{ nm}$  (or  $\sim 3.1 \text{ eV}$ ), and the Tauc plots provides a direct forbidden band gap of  $3.58 \text{ eV}$  (Fig. S6†) close to the reported value of  $3.59 \text{ eV}$ .<sup>29</sup> The Sb(III)-surface modification causes redshift in the absorption edge of which amount increases with an increase in  $\Gamma_{\text{ad}}$  from  $\sim 400 \text{ nm}$  at  $\Gamma_{\text{ad}} = 0$  to  $\sim 500 \text{ nm}$  at  $\Gamma_{\text{ad}} = 0.56 \text{ mmol g}^{-1}$ . To clarify the origin for the Sb(III)-surface modification-induced absorption, density functional theory (DFT) calculations were carried out for  $[\text{Sn}_{12}\text{O}_{25}]\text{-(SbCl)}_2$  used as a model of

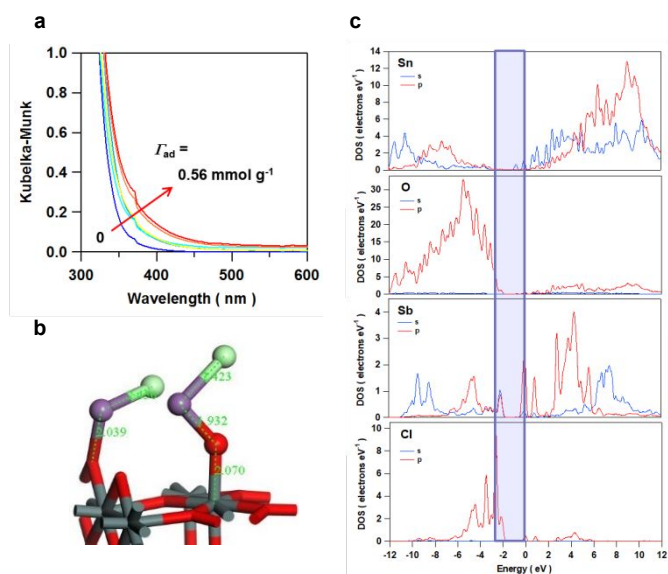


**Fig. 3.** (a) Absorption spectra of  $\text{SnO}_2\text{-Sb(III)}$  NCs with varying  $\Gamma_{\text{ad}}$ . (b) Optimized structure of  $[\text{Sn}_{12}\text{O}_{25}]\text{-(SbCl)}_2$ . (c) PEDOS of  $[\text{Sn}_{12}\text{O}_{25}]\text{-(SbCl)}_2$ . Pale purple region expresses the band gap of unmodified  $\text{SnO}_2$ .

$\text{SnO}_2\text{-Sb(III)}$ . In this model,  $\text{SbCl}$  was bonded to the O atom on the most stable  $\text{SnO}_2(110)$  plane.<sup>30</sup> The DFT-optimized structure of  $[\text{Sn}_{12}\text{O}_{25}]\text{-(SbCl)}_2$  and the projected electronic density of states (PEDOS) are shown, where the pale purple region expresses the band gap of unmodified  $\text{SnO}_2$  (Fig. 3b,c). The CB minimum and VB maximum of unmodified  $\text{SnO}_2$  consist of  $\text{Sn}5s\text{-}5p$  and  $\text{O}2p$  orbitals, respectively. The band gap of  $\sim 3 \text{ eV}$  is close to the absorption edge energy ( $\sim 3.1 \text{ eV}$ ) rather than the direct forbidden band gap ( $3.58 \text{ eV}$ ). These results indicate that the Sb(III)-surface modification of  $\text{SnO}_2$  generates the surface levels consisting of  $\text{Sb}5s\text{-}5p$  and  $\text{Cl}3p$  orbitals

above the VB maximum of  $\text{SnO}_2$  to induce the band gap narrowing and the visible-light absorption.

$\text{SnO}_2$  NC films without and with the Sb(III)-surface modification were formed on fluorine-doped tin oxide electrodes ( $\text{SnO}_2/\text{FTO}$ ,  $\text{SnO}_2\text{-Sb(III)/FTO}$ ). Electrochemical properties of the  $\text{SnO}_2/\text{FTO}$  and  $\text{SnO}_2\text{-Sb(III)/FTO}$  electrodes for OER were studied by measuring the current ( $J$ )-potential ( $E$ ) curves in deaerated  $0.1 \text{ M NaClO}_4$  electrolyte solutions (pH 5.7) in the dark (dotted curves) and under visible-light irradiation ( $\lambda_{\text{ex}} = 420 \text{ nm}$ , solid curves) (Fig. 4a). In the dark, anodic current due to OER rises at  $E \approx 1.5 \text{ V}$  in each electrode. Visible-light irradiation of the  $\text{SnO}_2/\text{FTO}$  electrode hardly affects the current. On the contrary, in the  $\text{SnO}_2\text{-Sb(III)/FTO}$  electrode, significant photocurrent is induced with the onset potential shift to  $0 \sim +0.1 \text{ V}$ . The value reduced at pH 0 ( $+0.34 \sim +0.44 \text{ V}$ ) is close to the CB-edge potential of  $\text{SnO}_2$  ( $+0.48 \text{ V}$  at pH 0).<sup>31</sup> This is consistent with the DFT-simulation results that the CB minimum of  $\text{SnO}_2$  is hardly affected by the Sb(III)-surface modification (Fig. 3c). Photochronoamperometry curves were measured for the  $\text{SnO}_2\text{-Sb(III)/FTO}$  electrodes at the rest potential in the dark (Fig. 4b). In the  $J$  vs.  $\Gamma_{\text{ad}}$  plots (Fig. 4c), the photocurrent initially rises with increasing  $\Gamma_{\text{ad}}$  to slowly decrease through a maximum at  $\Gamma_{\text{ad}} = 0.18 \text{ mmol g}^{-1}$ . Further, in the action spectrum of the photocurrent for OER over the  $\text{SnO}_2\text{-Sb(III)/FTO}$  electrode (Fig. 4d), the photocurrent rises at  $\lambda_{\text{ex}} \sim 470 \text{ nm}$  to increase as the  $\lambda_{\text{ex}}$  becomes shorter, and the profile of the action spectrum well traces the absorption spectrum of  $\text{SnO}_2\text{-Sb(III)}$  NCs. Evidently, the Sb(III)-surface modification endows  $\text{SnO}_2$  with the visible-induced OER ability.

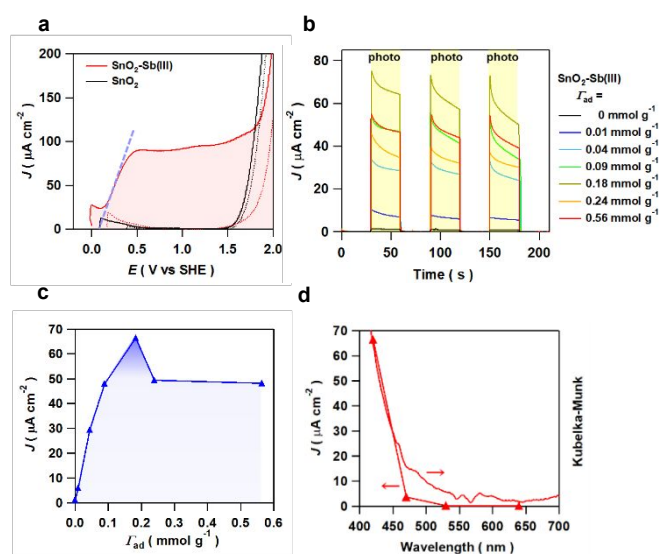


**Fig. 4.** (a) Current ( $J$ )-potential ( $E$ ) curves for  $\text{SnO}_2/\text{FTO}$  and  $\text{SnO}_2\text{-Sb(III)/FTO}$  electrodes in deaerated  $0.1 \text{ M NaClO}_4$  electrolyte solution (pH 5.7) in the dark and under visible-light irradiation ( $\lambda_{\text{ex}} = 420 \text{ nm}$ ,  $8.1 \text{ mW cm}^{-2}$ ). (b) Photochronoamperometry curves of  $\text{SnO}_2\text{-Sb(III)/FTO}$  electrodes with varying  $\Gamma_{\text{ad}}$  at the rest potential in the dark. (c) Plots of  $J$  vs.  $\Gamma_{\text{ad}}$ . (d) Action spectrum for the photocurrent of the  $\text{SnO}_2\text{-Sb(III)/FTO}$  electrode. The absorption spectrum is also shown for comparison.

Au NPs (loading amount  $x_{\text{Au}} = 2.66$  mass%) were deposited on  $\text{SnO}_2$  NCs by the deposition precipitation (DP) method,<sup>32</sup> and then,  $\text{SbCl}_3$  was chemisorbed on the sample. The d-spacing of the lattice fringe in the deposit (2.36 Å) in the HR-TEM image (Fig. 5a) is in agreement with the value of Au(111) (2.355 Å) (ICDD No. 00-004-0784). In the absorption spectra of  $\text{Au@SnO}_2\text{-Sb(III)}$  (Fig. 5b), new absorption due to the localized surface plasmon resonance (LSPR) appears around 550 nm with Au NP-loading on  $\text{SnO}_2\text{-Sb(III)}$ . As shown in the TEM-EDS elemental mapping (Fig. 5c), a single Au NP (~50 nm) is present on a cluster (~500 nm) of many  $\text{SnO}_2\text{-Sb(III)}$  NCs with a primary particle size of ~30 nm ( $\text{Au@SnO}_2\text{-Sb(III)}$ ). Intriguingly, every  $\text{SnO}_2$  cluster contains ~one Au NP (Fig. S7†). The HR-TEM image for the  $\text{SnO}_2$  cluster shows that  $\text{SnO}_2$  NCs are interconnected through an epitaxial junction with the (101) <sub>$\text{SnO}_2$</sub> //(101) <sub>$\text{SnO}_2$</sub>  orientation (Fig. S8†). Downsizing Au particle below 5 nm causes a steep decrease in its melting point ( $T_m$ ) from  $T_m \approx 1100$  K at Au particle size ( $d_{\text{Au}}$ ) = 5 nm to  $T_m \approx 700$  K at  $d_{\text{Au}} = 2$  nm.<sup>33</sup> In the DP method, small Au NPs are initially generated during the heating process at temperature ( $T_c$ ) = 773 K, and the surface diffusion on the cluster of  $\text{SnO}_2$  NCs would be greatly enhanced finally to be fused into a single Au NP (~50 nm). For comparison, Au NPs were loaded on  $\text{SnO}_2$  NPs consisting of isolated particles (~100 nm) by the DP method, and  $\text{SbCl}_3$  were adsorbed on the samples ( $\text{Au/SnO}_2\text{-Sb(III)}$ ). Au NPs are dispersed on the surface of  $\text{SnO}_2$  NPs in  $\text{Au/SnO}_2\text{-Sb(III)}$  (Fig. S9†) as observed for the usual Au/MOs.<sup>34</sup>

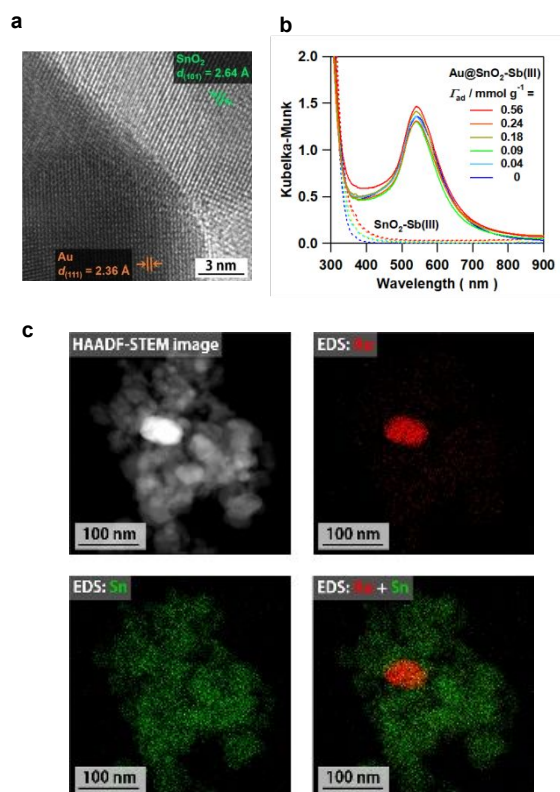


**Fig. 5.** (a) HR-TEM image of  $\text{Au@SnO}_2\text{-Sb(III)}$  prepared at  $C_0 = 50$  mM. (b) Absorption spectra of  $\text{Au@SnO}_2\text{-Sb(III)}$  (solid lines) and  $\text{SnO}_2\text{-Sb(III)}$  (dotted lines) with varying  $I_{\text{ad}}$ . (c) TEM-EDS mapping of  $\text{Au@SnO}_2\text{-Sb(III)}$  prepared at  $C_0 = 50$  mM.

The visible-light activities of various samples for  $\text{H}_2\text{O}_2$  generation from air-saturated water were evaluated (Fig. 6a). While  $\text{SnO}_2$  and

$\text{Au/SnO}_2$  NCs are inactive,  $\text{SnO}_2\text{-Sb(III)}$  NC yields  $\text{H}_2\text{O}_2$  with an initial rate ( $v_0\text{-H}_2\text{O}_2$ ) of  $0.9$   $\text{mM h}^{-1} \text{g}^{-1}$ . Strikingly, loading Au NPs on  $\text{SnO}_2\text{-Sb(III)}$  NCs enhances the  $v_0$  value to  $6.1$   $\text{mM h}^{-1} \text{g}^{-1}$ , while no  $\text{H}_2\text{O}_2$  is formed without  $\text{O}_2$ .  $\text{O}_2$  gas bubbling of the reaction solution was confirmed to hardly affect the rate of  $\text{H}_2\text{O}_2$  generation probably because it is limited by OER. The time courses for  $\text{H}_2\text{O}_2$  generation in the  $\text{Au/SnO}_2\text{-Sb(III)}$  and  $\text{Au@SnO}_2\text{-Sb(III)}$  systems (Fig. 6b) show the comparable initial rates. In the  $\text{Au/SnO}_2\text{-Sb(III)}$  system, the photocatalytic activity decreases with the passage of reaction time. In contrast, in the  $\text{Au@SnO}_2\text{-Sb(III)}$  system, the concentration of  $\text{H}_2\text{O}_2$  increases in proportion to irradiation time. This marked difference partly stems from the catalytic activity of  $\text{Au@SnO}_2\text{-Sb(III)}$  much lower than  $\text{Au/SnO}_2\text{-Sb(III)}$  for  $\text{H}_2\text{O}_2$  decomposition (Fig. 6c). The rate of  $\text{H}_2\text{O}_2$  generation is further boosted from  $6.1$   $\text{mM g}^{-1}$  to  $20$   $\text{mM g}^{-1}$  under illumination of simulated sunlight (AM-1.5, one sun) (Fig. S10†). The photocatalytic activity of  $\text{Au@SnO}_2\text{-Sb(III)}$  exceeds the values for most of the state-of-the-art inorganic photocatalysts for  $\text{H}_2\text{O}_2$  synthesis from water and  $\text{O}_2$  (Table S1†). Very recently, an exceptionally high photocatalytic activity of  $\sim 59.4$   $\text{mM g}^{-1} \text{h}^{-1}$  has been reported for  $\text{H}_2\text{O}_2$  photosynthesis using a faceted  $\text{BiVO}_4$ -based photocatalyst.<sup>20</sup> However, the  $\text{H}_2\text{O}_2$ -generating rate decreases with reaction time because of the high affinity of  $\text{BiVO}_4$  for  $\text{H}_2\text{O}_2$  (Fig. 1 lower, Table S2†). The plot of the photocatalytic activity of  $\text{Au@SnO}_2\text{-Sb(III)}$  and the photocurrent of the  $\text{SnO}_2\text{-Sb(III)/FTO}$

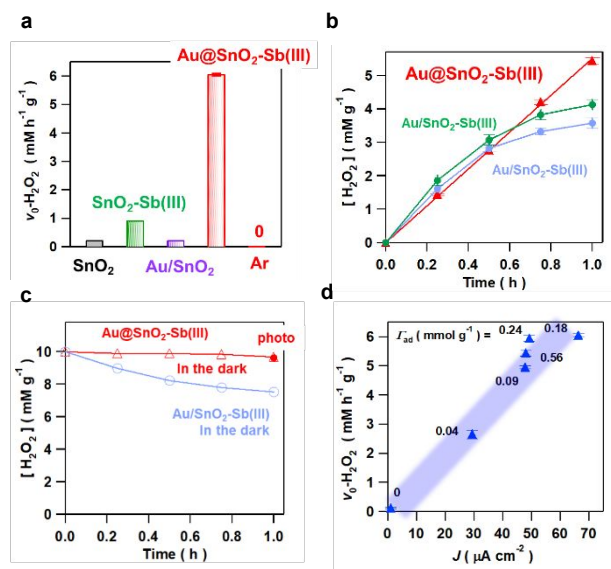
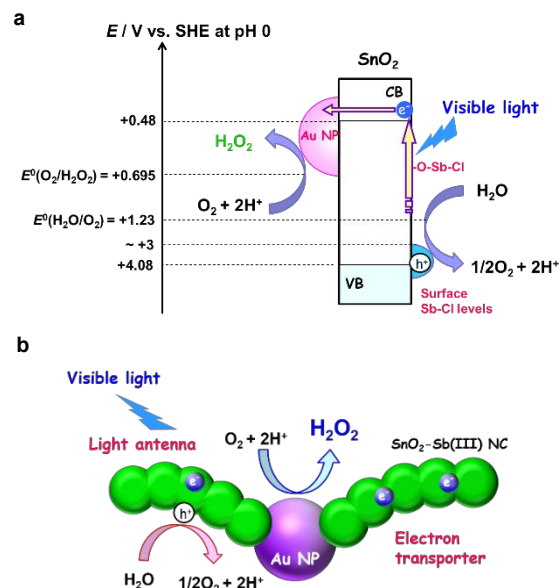


**Fig. 6.** (a) Comparison of the photocatalytic activity of  $\text{SnO}_2$ ,  $\text{SnO}_2\text{-Sb(III)}$  ( $I_{\text{ad}} = 0.18$   $\text{mmol g}^{-1}$ ),  $\text{Au/SnO}_2$ , and  $\text{Au@SnO}_2\text{-Sb(III)}$  ( $I_{\text{ad}} = 0.18$   $\text{mmol g}^{-1}$ ) for  $\text{H}_2\text{O}_2$  generation from air-saturated water under visible-light irradiation ( $\lambda_{\text{ex}} = 420$  nm) at 298 K. (b) Time courses for the photocatalytic  $\text{H}_2\text{O}_2$  generation from air-saturated water in the  $\text{Au@SnO}_2\text{-Sb(III)}$  and  $\text{Au/SnO}_2\text{-Sb(III)}$  with  $d_{\text{Au}} = 6.4$  nm,  $x_{\text{Au}} = 2.59$  mass% (green) and  $d_{\text{Au}} = 3.1$  nm,  $x_{\text{Au}} = 2.66$  mass% (blue) systems under irradiation ( $\lambda_{\text{ex}} = 420$  nm) at 298 K. (c) Time courses for  $\text{H}_2\text{O}_2$  decomposition by  $\text{Au@SnO}_2\text{-Sb(III)}$  ( $I_{\text{ad}} = 0.18$   $\text{mmol g}^{-1}$ ) in the dark or under visible-light irradiation ( $\lambda_{\text{ex}} = 420$  nm) or by  $\text{Au/SnO}_2\text{-Sb(III)}$  ( $I_{\text{ad}} = 0.18$   $\text{mmol g}^{-1}$ ) in the dark at 298 K. (d) The relation between the photocatalytic activity of  $\text{Au@SnO}_2\text{-Sb(III)}$  with varying  $I_{\text{ad}}$  for  $\text{H}_2\text{O}_2$  generation and the photocurrent of the  $\text{SnO}_2\text{-Sb(III)}$  electrodes at the rest potential in the dark.

electrode provides a positive correlation between them (Fig. 6d), indicating that the OER is the key step in this reaction. To check the stability of Au@SnO<sub>2</sub>-Sb(III), the photocatalytic reaction was repeated under the same conditions. The photocatalytic activity is maintained even after the reaction was repeated 5 times (Fig. S11a†). Further, the absorption spectra (Fig. S11b†) and XP spectra (Fig. S12†) of Au@SnO<sub>2</sub>-Sb(III) show that not only the amounts of Sb and Au but also the states hardly change before and after the repeated reaction. The external quantum yield ( $\phi_{\text{ex}}$ ) for the reaction in the Au@SnO<sub>2</sub>-Sb(III) system reaches 1.1% at  $\lambda_{\text{ex}} = 420$  nm (Fig. S13†), and the action spectrum is similar to that of the photocurrent (Fig. 4d), strongly suggesting that this reaction is induced by the excitation of not the LSPR of Au NPs but SnO<sub>2</sub>-Sb(III) NCs. Also, SnO<sub>2</sub> has broad emission around 440 nm due to the surface vacancy in the photoluminescence (PL) spectrum (Fig. S14†),<sup>35</sup> and the spectrum hardly changes with the Sb(III)-surface modification. A significant decrease in the signal intensity is observed with the loading of Au NPs in spite that the unit structure of Au@SnO<sub>2</sub>-Sb(III) has only ~one Au NP. In this system, the excited electrons can be transported and collected to a single Au NP from the surrounding SnO<sub>2</sub> NCs interconnected each other.

On the basis of the energy diagram (Scheme 1a), the action mechanism of Au@SnO<sub>2</sub>-Sb(III) for the photocatalytic H<sub>2</sub>O<sub>2</sub> synthesis from water and O<sub>2</sub> is discussed in terms of the analogy with the natural photosynthesis (Scheme 1b). Excitation of Au@SnO<sub>2</sub>-Sb(III) by photons with  $\lambda_{\text{ex}} = 420$  nm promotes the electrons in the Sb(III)-induced levels above the VB of SnO<sub>2</sub> to the CB of SnO<sub>2</sub>. The holes generated in the Sb(III)-surface levels oxidize water to yield O<sub>2</sub> and H<sup>+</sup> without the diffusion to the surface and with the assistance by the photoelectrocatalytic activity. On the other hand, a recent electrochemical study using Au/fluorine-doped SnO<sub>2</sub> rotating electrode have shown that Au NPs loaded on SnO<sub>2</sub> possess electrocatalytic activity for 2e<sup>-</sup>-ORR.<sup>36</sup> Thus, H<sup>+</sup>-coupled 2e<sup>-</sup>-ORR effectively proceeds on the surface of Au NP with the aid of the electrocatalytic activity,<sup>25,37</sup> generating the concentration gradient of the excited electrons in the SnO<sub>2</sub> NCs towards the radial direction of Au NP to be the driving force for the one-directional electron transport in the functional unit of Au@SnO<sub>2</sub>-Sb(III). Consequently, the excited electrons in the cluster of SnO<sub>2</sub>-Sb(III) NCs are transported and collected to a single Au NP via the interparticle electron transport through the high-quality interface, and effective charge separation is achieved. The electron transport between SnO<sub>2</sub> NPs was previously utilized for the photoanode of quantum dot-sensitized solar cells.<sup>38</sup> Although the Sb(III)-surface modification somewhat increases the adsorptivity of SnO<sub>2</sub> for H<sub>2</sub>O<sub>2</sub>, it is still much weaker than the other MOs (Table S2†), and the decomposition of H<sub>2</sub>O<sub>2</sub> once generated can be suppressed over SnO<sub>2</sub>-Sb(III). In this case, the importance of the large Au particle size ( $d_{\text{Au}} = \sim 50$  nm) in Au@SnO<sub>2</sub>-Sb NCs should be emphasized. In the Au/semiconductor photocatalysts, the charge separation through the interfacial electron transfer from the semiconductor to Au NP is enhanced with increasing Au particle size.<sup>39</sup> Although Au NP shows the catalytic activity for H<sub>2</sub>O<sub>2</sub> decomposition, the activity decreases with increasing Au particle size and negligibly small at  $d_{\text{Au}} > 12$  nm.<sup>25</sup> In addition, the robustness of each component in the photocatalyst and the strong chemical bond between the SbCl species and SnO<sub>2</sub> would lead to the stable production of H<sub>2</sub>O<sub>2</sub>. In this manner, Au@SnO<sub>2</sub>-Sb(III) fulfils the requirements (1)-(6) to exhibit the remarkable photocatalytic activity and stability for the production of H<sub>2</sub>O<sub>2</sub> from water and O<sub>2</sub> under



**Scheme 1.** (a) The energy diagram of Au@SnO<sub>2</sub>-Sb(III) was constructed by assuming that the CB edge potential of SnO<sub>2</sub> is approximated by the flat band potential of +0.48 V (SHE at pH 0).<sup>31</sup> The VB maximum potential and the top of the surface levels due to the SbCl species were estimated from the band gap of SnO<sub>2</sub> and the absorption edge of SnO<sub>2</sub>-Sb(III) to be 4.08 V and ~+3 V, respectively. (b) Analogy with the natural photosynthetic system.

visible-light irradiation. Compared this system to the natural photosynthetic system, the cluster of SnO<sub>2</sub>-Sb(III) NCs acts as “light harvester (antenna chlorophylls)”, “electron transporter and collector (light energy transporter and collector in antenna chlorophylls)” and “oxidation reaction end (P680)”, while Au NP operates as “reduction reaction end (P700)”.

## Conclusions

This study has shown that visible-light irradiation ( $\lambda_{\text{ex}} = 420$  nm) of Au@SnO<sub>2</sub>-Sb(III) stably yields H<sub>2</sub>O<sub>2</sub> from water and O<sub>2</sub> with a rate of 6.1 mM g<sup>-1</sup> h<sup>-1</sup> and an external quantum yield of 1.10%. Au@SnO<sub>2</sub>-Sb(III) has a unique unit structure consisting of a single Au NP (~50 nm) and a cluster (> 150 nm) of SnO<sub>2</sub>-Sb(III) NCs (~30 nm). The remarkable activity stems from the efficient charge separation through the interparticle electron transfer from SnO<sub>2</sub>-Sb(III) NCs to a single Au NP, the electrocatalytic activity of Au NPs for 2e<sup>-</sup>-ORR, the visible light-induced activity of SnO<sub>2</sub>-Sb(III) for OER, the weak adsorptivity of SnO<sub>2</sub>-Sb(III) for H<sub>2</sub>O<sub>2</sub>, and the low catalytic activity of large Au NP for H<sub>2</sub>O<sub>2</sub> decomposition. We believe that this study would pave the way of a new biomimetic design of highly active robust inorganic nanohybrid photocatalysts for the solar-to-chemical conversion.

## Data availability

The data supporting the findings can be found in the article and ESI, and are available from the authors upon reasonable request.

## Author Contributions

M. T., S. N., and Y. Y. conducted catalysts synthesis, characterization, and photocatalytic reaction experiments, T. S. performed TEM observation and analysis, H. K. performed DFT simulations, and H. T. supervised the work and data analysis.

## Conflicts of interest

There are no conflicts to declare.

## Acknowledgements

This work was financially supported by JST Adaptable and Seamless Technology Transfer Program through Target-driven R&D, JSPS KAKENHI Grant-in-Aid for Scientific Research (C) no. 20K05275, 20K05674, and 21K05236, the Futaba Foundation, Nippon Sheet Glass Foundation for Materials Science and Engineering, Sumitomo Foundation, Takahashi Industrial and Economic Research Foundation.

## Notes and references

- R. Noyori, M. Aoki and K. Sato, *Chem. Commun.*, 2003, **39**, 1977-1986.
- D. B. Miklos, C. Remy, M. Jekel, K. G. Linden, J. E. Drewes and U. Hübner, *Water Res.*, 2018, **139**, 118-131.
- S.-i. Yamazaki, Z. Siroma, H. Senoh, T. Iori, N. Fujiwara and K. A. Yasuda, *J. Power Sources*, 2008, **178**, 20-25.
- Y. Yamada, S. Yoshida, T. Honda and S. Fukuzumi, *Energy Environ. Sci.*, 2011, **4**, 2822-2825.
- A. M. Shaegh, N.-T. Nguyen, S. M. M. Ehteshami and S. H. Chan, *Energy Environ. Sci.*, 2012, **5**, 8225-8228.
- K. Mase, M. Yoneda, Y. Yamada and S. Fukuzumi, *Nat. Commun.*, 2016, **7**, 11470.
- J. M. Campos-Martin, G. Blanco-Brieva and J. L. G. Fierro, *Angew. Chem. Int. Ed.*, 2006, **45**, 6962-6984.
- H. Hou, X. Zeng and X. Zhang, *Angew. Chem. Int. Ed.*, 2020, **59**, 17356-17376.
- H. Tada, *Nanoscale Adv.*, 2019, **1**, 4238-4245.
- S. Wu and X. Quan, *ACS EST Eng.*, 2022 DOI: 10.1021/acsestengg.1c00546, and the references therein.
- Q. Tian, L. Jing, S. Ye, J. Liu, R. Chen, C. A. H. Price, F. Fan and J. Liu, *Small*, 2012, **17**, 2103224, and the references therein.
- J. Xiao, Q. Han, Y. Xie, J. Yang, Q. Su, Y. Chen and H. Cao, *Environ. Sci. Technol.*, 2017, **51**, 13380-13387.
- L. Wang, J. Zhang, Y. Zhang, H. Yu, Y. Qu and J. Yu, *Small*, 2022, **18**, 2104561, and the references therein.
- N. Kaynan, B. A. Berke, O. Hazut and R. Yerushalmi, *J. Mater. Chem. A.*, 2014, **2**, 13822-13826.
- H. Hirakawa, S. Shiota, Y. Shiraishi, H. Sakamoto, S. Ichikawa and T. Hirai, *ACS Catal.*, 2016, **6**, 4976-4982.
- Y. Wang, Y. Wang, J. Zhao, M. Chen, X. Huang and Y. Xu, *Appl. Catal. B*, 2021, **284**, 119691/1-11.
- W.-C. Hou and Y.-S. Wang, *ACS Sustain. Chem. Eng.*, 2017, **5**, 2994-3001.
- W. Zhang, X. Chen, X. Zhao, M. Yin, L. Feng and H. Wang, *Appl. Surf. Sci.*, 2020, **527**, 146908/1-9.
- W. Xie, Z. Huang, R. Wang, C. Wen and Y. Zhou, *J. Mater. Sci.*, 2020, **55**, 11829-11840.
- T. Liu, Z. Pan, J. J. M. Vequizo, K. Kato, B. Wu, A. Yamakata, K. Katayama, B. Chen, C. Chu and K. Domen, *Nat. Commun.*, 2022, **13**, 1034/1-8.
- L. Yang, D. Fan, Z. Li, Y. Cheng, X. Yang and T. Zhang, *Adv. Sustain. Syst.*, 2022, **6**, 2100477.
- Electrochem. Soc. Jpn. Ed., *Denkikagaku Binran (Handbook of Electrochemistry)*, Maruzen, Tokyo, 2000.
- S. Zhao, X. Zhao, *Appl. Catal. B*, 2019, **250**, 408-418.
- X. Li, C. Chen, J. Zhao, *Langmuir*, 2001, **17**, 4118-4122.
- M. Teranishi, S. Naya and H. Tada, *J. Am. Chem. Soc.*, 2010, **132**, 7850-7851.
- K. Kim, J. Park, H. Kim, G. Y. Jung, M.-G. Kim, *ACS Catal.*, 2019, **9**, 9206-9211.
- D. Tsukamoto, A. Shiro, Y. Shiraishi, Y. Sugano, S. Ichikawa, S. Tanaka, T. Hirai, *ACS Catal.*, 2012, **2**, 599-603.
- XPS database, <http://techdb.podzone.net/>
- M. Voinov and J. Augustynski, *Heterogeneous Photocatalysis*, Edited by Schiavello, M. John Wiley & Sons, New York 1997.
- J. Oviedo and M. J. Gillan, *Surf. Sci.*, 2000, **463**, 93-101.
- H. Tada, A. Hattori, Y. Tokihisa, K. Imai, N. Tohge and S. Ito, *J. Phys. Chem. B*, 2000, **104**, 4585-4587.
- S. Tsubota, M. Haruta, T. Kobayashi, A. Ueda and Y. Nakahara, *Preparation of catalysts V*, Elsevier, Amsterdam, 1991.
- P. Buffat and J.-P. Borel, *Phys. Rev. A*, 1976, **13**, 2287-2298.
- T. Ishida, T. Maruyama, A. Taketoshi and M. Haruta, *Chem. Rev.*, 2020, **120**, 464-525.
- X. Zhang, F. Guo, L. Zhuang, Q. Jin and X. Zhang, *Opt. Quantum Electronics*, 2022, **54**, 82/1-12.
- T. Kunimoto, S. Naya and H. Tada, *Chem. Lett.*, 2021, **50**, 1589-1591.
- C. M. Sánchez-Sánchez and A. J. Bard, *Anal. Chem.*, 2009, **81**, 8094-8100.
- K. Tvrđy, P. A. Frantsuzov and P. V. Kamat, *Proc. Natl. Acad. Sci.*, 2011, **108**, 29-34.
- H. Tada, T. Kiyonaga and S. Naya, *Chem. Soc. Rev.*, 2009, **38**, 1849-1858.